

STIRAP-inspired robust gates for a superconducting dual-rail qubit

Ujjawal Singhal,¹ Harsh Vardhan Upadhyay,¹ Irshad Ahmad,¹ and Vibhor Singh^{1,*}

¹*Department of Physics, Indian Institute of Science, Bangalore-560012 (India)*

(Dated: October 8, 2024)

STImulated Raman Adiabatic Passage (STIRAP) is a powerful technique for robust state transfer capabilities in quantum systems. This method, however encounters challenges for its implementation as a gate in qubit-subspace due to its sensitivity to initial states. By incorporating single-photon detuning into the protocol, the sensitivity to the initial state can effectively be mitigated, enabling STIRAP to operate as a gate. In this study, we experimentally demonstrate the implementation of robust π and $\pi/2$ rotations in a dual-rail qubit formed by two strongly coupled *fixed-frequency* transmon qubits. We achieve state preparation fidelity in excess of 0.98 using such rotations. Our analysis reveals these gates exhibit significant resilience to errors. Furthermore, our numerical calculations confirm that these gates can achieve fidelity levels in excess of 0.999. This work suggest a way for realizing quantum gates which are robust against minor drifts in pulse or system parameters.

INTRODUCTION

Accurate and efficient control over a quantum system is essential for developing robust quantum computing platforms. Typically, such control is achieved by driving the system with *resonant* pulses and manipulating their parameters like amplitude, phase, and frequency. On one hand, while resonant interactions are accurate, they are also highly sensitive to parameter variations. Adiabatic evolution techniques, on the other hand, offer greater robustness against minor drifts in both *pulse* and *system* parameters [1, 2]. STIRAP is a powerful technique among adiabatic protocols and it has been widely used for population transfer and precision measurements across various systems such as Rydberg atoms, trapped ions, and various solid-state systems including superconducting qubits [3–8].

While STIRAP protocols are highly robust for population transfer and creating superposition states [9], they do not directly constitute quantum gates due to their sensitivity to the initial state [3, 4]. This limitation can be overcome with modifications to the protocol. For instance, introducing a non-zero single-photon detuning and using fractional-STIRAP with back-to-back pulses can lead to robust swap gates [10–12]. Additionally, using auxiliary levels can facilitate the realization of rotations in the qubit subspace [13, 14].

In the case of superconducting qubits, there is recent interest in developing STIRAP-inspired gates to connect states with low transition dipoles [15, 16]. Such protocols have also been investigated for implementing one- and two-qubit gates, contributing to the broader class of geometric quantum gates [17–22]. However, STIRAP and its super-adiabatic variants have been experimentally utilized to demonstrate the population transfer in a single superconducting qubit [5–8]. Thus far, their application as a quantum gate in superconducting platform has remain unexplored.

Recently, resonantly coupled transmons have been used to realize dual-rail qubits, where the computa-

tional subspace is spanned by the symmetric and anti-symmetric combinations of the single-excitation states [23, 24]. Due to the low transition dipole of the two "logical" states, the dual-rail qubit exhibits higher coherence times, as the reduced dipole suppresses direct radiative transitions. It also makes it challenging to drive the qubit with a resonant pulse. Thus, a dual-rail qubit could be a suitable platform for testing the performance of STIRAP-inspired quantum gates. So far, the single-qubit gates in dual-rail qubit have been implemented by designing one of the qubits to be flux-tunable and modulating its frequency [24, 25].

In this work, we demonstrate STIRAP-inspired gates in a dual-rail qubit, marking the experimental realization of both π and $\pi/2$ gates in superconducting qubits using detuned STIRAP. While π rotations using detuned STIRAP have been theoretically proposed, our study represents the experimental demonstration of such gates. Additionally, we extend this methodology to implement $\pi/2$ gates using detuned STIRAP, which have not been explored earlier. By employing large single-photon detuning, we achieve robust gate operations. These gate operations are validated through quantum state tomography, and their performance is evaluated with respect to deviations in Rabi amplitude and frequency. It is interesting to remark that while the protocol operates within a single-qubit subspace, it is inherently a two-qubit operation in the individual qubit basis. In our protocol, the use of the common ground state as an auxiliary level, and two microwave pulses can reduce the hardware requirements and minimize environmental noise in a dual-rail qubit architecture.

The paper is organized as follows: we first provide a brief overview of the STIRAP protocol to establish notation and to convey the basic idea. Next, we discuss the case of detuned STIRAP, showing how detuning in the control signals enables single-qubit rotations in a subspace spanned by a three-level system while maintaining partial adiabaticity. We then present experimental results, discussing the single qubit rotations on Bloch

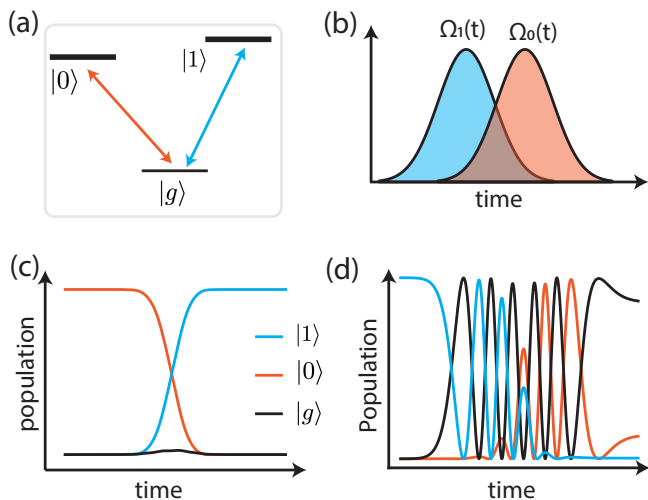


FIG. 1. **Schematic of resonant STIRAP** (a) A schematic of the V-type 3-level system consisting of a ground state $|g\rangle$, and two excited states $|0\rangle$ and $|1\rangle$. (b) A schematic of a counter-intuitive pulse ordering for the transfer of population from $|0\rangle$ to $|1\rangle$. (c) Time-evolution of the populations in different levels for the resonant STIRAP when the initial state is $|0\rangle$. Ultimately, it leads to a complete transfer of population to $|1\rangle$. (d) The evolution when the initial state is $|1\rangle$. The oscillations show the mixing between the three states as the system evolves.

sphere and their robustness to control pulse parameters.

THEORETICAL MODEL

Brief overview of STIRAP

STIRAP is a control technique allowing complete population transfer between two uncoupled states via one or more intermediate states that are never populated ideally. Consider a general “V-type” system comprising of two orthogonal excited states, denoted by $|0\rangle$ and $|1\rangle$, and a ground state denoted as $|g\rangle$ as shown in Fig. 1(a). The transitions $|g\rangle \leftrightarrow |0\rangle$ and $|g\rangle \leftrightarrow |1\rangle$ can be driven by two-time dependent signals $\Omega_0(t) \cos \omega_0 t$ and $\Omega_1(t) \cos \omega_1 t$. The control signals are characterized by slowly varying Rabi amplitudes $\Omega_0(t)$ and $\Omega_1(t)$ as shown in Fig. 1(b). Here, ω_0 and ω_1 are the transition frequencies corresponding to $|g\rangle \leftrightarrow |0\rangle$ and $|g\rangle \leftrightarrow |1\rangle$ transitions, respectively.

By performing the rotating wave transformation to eliminate the fast-time dependence on the control fields, it is straightforward to obtain the following Hamiltonian with $\hbar = 1$,

$$H(t) = \frac{1}{2} \begin{pmatrix} 0 & \Omega_0(t) & 0 \\ \Omega_0(t) & 2\Delta & \Omega_1(t) \\ 0 & \Omega_1(t) & 2\delta \end{pmatrix}, \quad (1)$$

where the detunings of the driving fields from the corresponding resonances are defined as $\Delta_p = \omega_{g0} - \omega_0$ and $\Delta_s = \omega_{g1} - \omega_1$ with the single-photon detuning given by $\Delta = (\Delta_p + \Delta_s)/2$, and the two-photon detuning $\delta = \Delta_p - \Delta_s$. Insight into the dynamics of the system can be made by setting the two-photon detuning $\delta = 0$. This leads to the following instantaneous eigenstate,

$$\begin{aligned} |+\rangle &= \sin \theta \sin \phi |0\rangle + \cos \theta \sin \phi |1\rangle + \cos \phi |g\rangle, \\ |-\rangle &= \sin \theta \cos \phi |0\rangle + \cos \theta \cos \phi |1\rangle - \sin \phi |g\rangle, \\ |d\rangle &= \cos \theta |0\rangle - \sin \theta |1\rangle, \end{aligned}$$

where the mixing angles θ and ϕ are given by $\theta(t) = \tan^{-1}(\Omega_0(t)/\Omega_1(t))$ and $2\phi(t) = \tan^{-1}(\Omega_{\text{rms}}(t)/\Delta)$ and $\Omega_{\text{rms}}(t) = \sqrt{|\Omega_0(t)|^2 + |\Omega_1(t)|^2}$. The corresponding eigenfrequencies are given by, $\varepsilon_{\pm}(t) = \frac{1}{2} (\Delta \pm \sqrt{\Delta^2 + \Omega_{\text{rms}}(t)^2})$, and $\varepsilon_d(t) = 0$. The eigenstate with zero eigenenergy, the dark state $|d\rangle$ is the key to understand the transfer process. When the system is initialised in state $|0\rangle$, the dark state $|d\rangle$ can be evolved adiabatically by changing the mixing angle $\theta(t)$ from 0 to $\pi/2$, as shown in Fig. 1(c).

It is important to note that when the single-photon detuning Δ and two-photon detuning δ is set to zero, it leads to a energy gap of $\Omega_{\text{rms}}(t)/2$ between the instantaneous eigenenergies of the dark state and the two other states. This gap facilitates adiabatic evolution through the dark state during the process, ultimately leading to population transfer from state $|0\rangle$ to state $|1\rangle$ without populating the intermediate state $|g\rangle$. If the system is initialized in $|1\rangle$, the same pulse sequence results in an evolution through an equal superposition of the $|+\rangle$ and $|-\rangle$ eigenstates. Due to this, the final state is very sensitive to the phase acquired by these two eigenstates during the evolution, making it difficult to achieve successful robust state transfer when the system is initialized in the state $|1\rangle$, as shown in Fig. 1(d). Thus, while the STIRAP protocol can be employed for directional state-transfer, it cannot work as a quantum gate between $|0\rangle$ and $|1\rangle$ due to its sensitivity to the initial state [12].

Implementation of single-qubit gates using detuned STIRAP

The limitation of resonant STIRAP as a quantum gate arises from the initial degeneracy between the instantaneous eigenstates $|+\rangle$ and $|-\rangle$, resulting in an equal overlap with these states when initialized in $|1\rangle$. To implement a STIRAP-inspired gate, this degeneracy can be partially removed by introducing moderate single-photon detunings. As a result, the state $|+\rangle$ can be adiabatically eliminated, and the final state evolves through $|d\rangle$, or $|-\rangle$ (or both). When starting in $|0\rangle$, the adiabatic evolution proceeds via the eigenstate $|d\rangle$, as per the usual STIRAP evolution. However for $|1\rangle$, the evolution takes

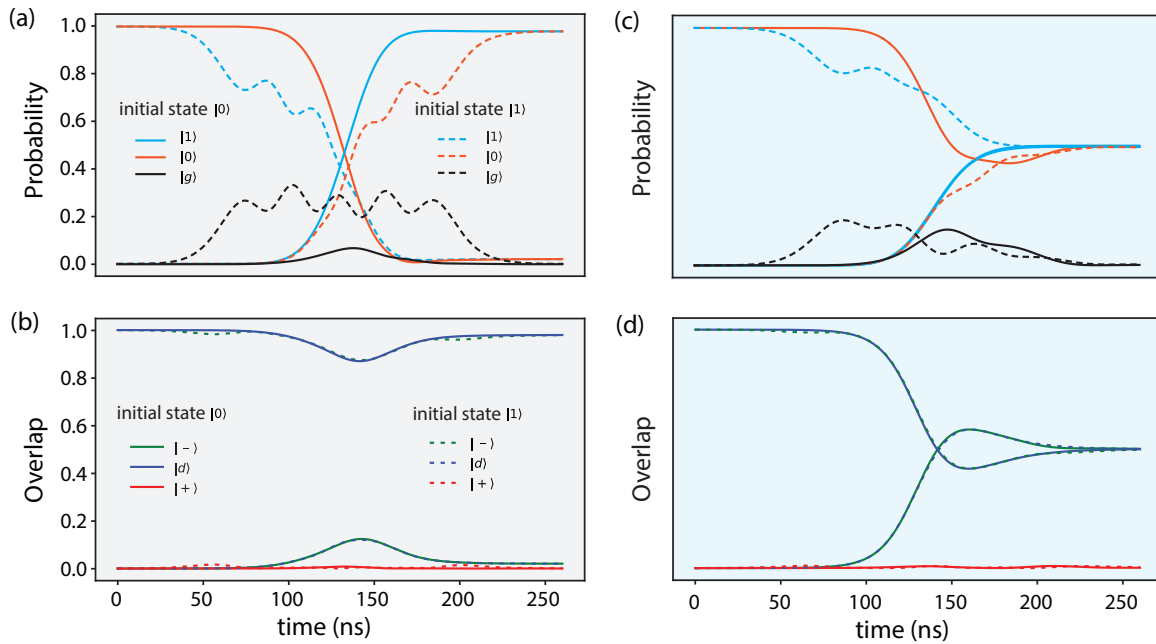


FIG. 2. **Time evolution for detuned STIRAP:** Evolution of states for the π gate and $\pi/2$ gate with non-zero single photon detuning ($\delta = 0$ MHz, $\Delta = 15$ MHz). The figures are plotted for two different initial states: solid lines represent evolution from the $|0\rangle$ initial state and dashed lines represent an evolution from the $|1\rangle$ initial state. (a) The population in different states during the evolution for the π rotation. (b) The overlap of the evolving state with the instantaneous eigenbasis for the π rotation. The evolution proceeds almost completely through a single eigenstate, $|d\rangle$ for the initial state $|0\rangle$ and $|-\rangle$ for the initial state $|1\rangle$. (c) The population in different states during the evolution for the $\pi/2$ rotation. (d) The evolution does not proceed through a single eigenstate for the $\pi/2$ rotation; instead, there is mixing between the eigenstates $|d\rangle$ and $|-\rangle$, making the $\pi/2$ rotation only partially adiabatic with adiabaticity being maintained with respect to the $|+\rangle$ eigenstate.

place via $|-\rangle$ eigenstate, while keeping the overlap with $|+\rangle$ suppressed. In this section, we give the theoretical framework of detuned STIRAP to better understand the π and $\pi/2$ rotations between the state $|0\rangle$ and $|1\rangle$.

To begin, we transform $H(t)$ to the adiabatic basis using the rotation matrix,

$$R(t) = \begin{pmatrix} \sin \theta(t) \sin \phi(t) & \cos \phi(t) & \cos \theta(t) \sin \phi(t) \\ \cos \theta(t) & 0 & -\sin \theta(t) \\ \sin \theta(t) \cos \phi(t) & -\sin \phi(t) & \cos \theta(t) \cos \phi(t) \end{pmatrix}. \quad (2)$$

In this frame, we obtain the effective Hamiltonian as,

$$\begin{aligned} H_{\text{ad}}(t) &= R(t)H(t)R^\dagger(t) - iR(t)\partial_t R^\dagger(t) \\ &= \begin{pmatrix} \epsilon_+(t) & \dot{\theta}(t) \sin \phi(t) & i\dot{\phi}(t) \\ -i\dot{\theta}(t) \sin \phi(t) & 0 & -i\dot{\theta}(t) \cos \phi(t) \\ -i\dot{\phi}(t) & i\dot{\theta}(t) \cos \phi(t) & \epsilon_-(t) \end{pmatrix}. \end{aligned} \quad (3)$$

Following the adiabatic theorem, the condition of adiabaticity, $\langle \psi_i | \dot{\psi}_j \rangle \ll |\epsilon_i - \epsilon_j|$, leads to the following conditions:

$$\left. \begin{aligned} |\dot{\phi}(t)| &\ll |\epsilon_+(t) - \epsilon_-(t)| \\ |\dot{\theta}(t) \sin(\phi(t))| &\ll |\epsilon_+(t)| \\ |\dot{\theta}(t) \cos(\phi(t))| &\ll |\epsilon_-(t)| \end{aligned} \right\} \quad (4)$$

where ψ_i represents one of the instantaneous eigenstates $\{|+\rangle, |-\rangle, |d\rangle\}$. To ensure the entire process remains adiabatic, all the conditions described in Eq. 4 must be satisfied throughout the evolution.

π rotations

To implement π rotations with respect to x or y -axes in the qubit subspace, we use the detuned STIRAP pulses by introducing a moderate single photon detuning. It leads to the adiabatic elimination of state $|+\rangle$. Now, let's consider the application of the detuned STIRAP pulses for two initial states $|0\rangle$ and $|1\rangle$. For the initial state $|0\rangle$, the instantaneous dark eigenstate at time $t = 0$ aligns perfectly with it. During the evolution under the detuned STIRAP pulses, the process remains nearly adiabatic, and the initial state evolves along $|d\rangle$ and ends up in $|1\rangle$ without populating the ground $|g\rangle$. Similarly, for the initial state $|1\rangle$, the instantaneous eigenstate $|-\rangle$ aligns

with it at time $t = 0$. Again, as the process is nearly adiabatic, the initial state will evolve along $|-\rangle$ and end up at $|0\rangle$.

Fig. 2(a) shows the results from numerical calculations based on QuTip [26], showing the probabilities in different eigenstates as the state of the system evolves. Further, by using the time-dependent Hamiltonian in Eq. 1, we found the instantaneous eigenstates ($|d(t)\rangle$, $|-(t)\rangle$ and $|+(t)\rangle$) at each point in time in the protocol. Afterwards, we evolve the initial states $|0\rangle$ and $|1\rangle$ with the protocol and found the overlap $|\langle i(t)|\psi(t)\rangle|^2$ during the evolution of the state, where $|i(t)\rangle \in \{|d(t)\rangle, |-(t)\rangle, |+(t)\rangle\}$, and $\psi(t)$ is the system's state during evolution.

Fig. 2(b) shows the results for two initial states $|0\rangle$ and $|1\rangle$. The evolution proceeds through the dark-state $|d\rangle$ and $|-\rangle$. We further emphasize that due to the separation of the eigenenergies, the process remains nearly adiabatic. The small dip during the evolution is due to the finite length of the process. Thus, as far as the transfers $|0\rangle \leftrightarrow |1\rangle$ are concerned, detuned STIRAP pulses perform a π rotation in the qubit subspace about some axis in the xy -plane.

In case of π rotations, it is also possible to analytically obtain the corresponding unitary. Using pulse parameters such that $\Omega_0 = \Omega_1 \lesssim \Delta$, the instantaneous eigenenergies always satisfy the adiabatic conditions given by Eq. 4. It implies that the off-diagonal coupling terms in H_{ad} are much smaller than the diagonal terms, thus leads to

$$H_{\text{ad}}(t) \simeq \begin{pmatrix} \epsilon_+(t) & 0 & 0 \\ 0 & 0 & 0 \\ 0 & 0 & \epsilon_-(t) \end{pmatrix}. \quad (5)$$

Given the diagonal form of $H_{\text{ad}}(t)$, we can write $U(t, 0) = R^\dagger(t) e^{-i \int_0^t H_{\text{ad}}(t') dt'} R(0)$, resulting in,

$$U(t, 0) = \begin{pmatrix} 0 & 0 & e^{-i\eta_-} \\ 0 & e^{-i\eta_+} & 0 \\ -1 & 0 & 0 \end{pmatrix}. \quad (6)$$

The phase factors in the above unitary are given by $\eta_- = \int_0^t \epsilon_-(t') dt'$ and $\eta_+ = \int_0^t \epsilon_+(t') dt'$.

The unitary in Eq. (6) represents a π rotation along an axis in the xy -plane. The specific axis of rotation can be controlled by adjusting the phases of the individual pulse envelopes. In particular, we modify the phase of both the detuned STIRAP pulse envelopes simultaneously: $\Omega_0(t) \rightarrow e^{i\beta} \Omega_0(t)$ and $\Omega_1(t) \rightarrow e^{i\beta} \Omega_1(t)$, where β is the phase shift applied to both pulses.

By tuning this phase β , we can align the axis of the π rotation to any desired direction in the xy -plane. This allows for the rotation to occur along the x -axis, y -axis, or any intermediate axis, depending on the chosen phase. Simultaneously adjusting the phases of the detuned STIRAP pulses in this way compensates for the accumulated

dynamical phase, thus enabling precise control over the π rotations about the x or y -axes.

$\pi/2$ rotations

Similar to the π rotations, $\pi/2$ rotations can also be implemented using the detuned STIRAP pulses. Using the pulse parameters $\Omega_0 = \Omega_1 < \Delta$, the state $|+\rangle$ can be adiabatically eliminated due to single-photon detuning. However, these pulse parameters do not comply with the last adiabatic condition in Eq. 4 and results in a partially adiabatic process. To understand $\pi/2$ rotations, we consider the time evolution of states, $|0\rangle$ and $|1\rangle$ under the application of detuned STIRAP pulses. These two states are aligned to either the dark state $|d\rangle$ or $|-\rangle$ at time $t = 0$. As the process is partially adiabatic, the initial state evolves involving both $|d\rangle$ and $|-\rangle$. Regardless of the initial state, under a suitable choice of pulse amplitude and equal superposition of $|0\rangle$ and $|1\rangle$ can be reached as shown in Fig. 2(c). It implies that the pulse sequence may perform a $\pi/2$ rotation along some axis in the xy -plane in the qubit subspace. Similar to the π rotations, the axis of the $\pi/2$ rotations can also be aligned along the x -axis or y -axis by adjusting the relative phase difference of the individual detuned STIRAP pulses.

As the process is not completely adiabatic, some of the off-diagonal terms in H_{ad} are not negligible when comparing to diagonal terms and Eq. 3 becomes,

$$H_{\text{ad}}(t) \simeq \begin{pmatrix} \epsilon_+(t) & 0 & 0 \\ 0 & 0 & -i\dot{\theta}(t) \cos \phi(t) \\ 0 & i\dot{\theta}(t) \cos \phi(t) & \epsilon_-(t) \end{pmatrix} \quad (7)$$

The non-negligible off-diagonal terms complicate the analytical calculation of unitary as $H_{\text{ad}}(t)$ does not commute with itself at different times. To get more details, we also compute the time evolution of instantaneous eigenstates. As expected, the evolution does not proceed through a single eigenstate, but there is a mixing between the eigenstates $|d\rangle$ and $|-\rangle$ as shown in Fig. 2(d). Therefore, the $\pi/2$ rotation protocol is only partially adiabatic, where adiabaticity is maintained with respect to the $|+\rangle$ eigenstate.

EXPERIMENTAL RESULTS

Device concept and basic characterization

Our device consists of two strongly coupled nearly identical transmon qubits, which results into one dipolar mode and one quadrupolar mode as shown schematically in Fig. 3(a). The device is fabricated on a sapphire substrate using Tantalum-based capacitor pads. Details of the device fabrication and measurement apparatus are

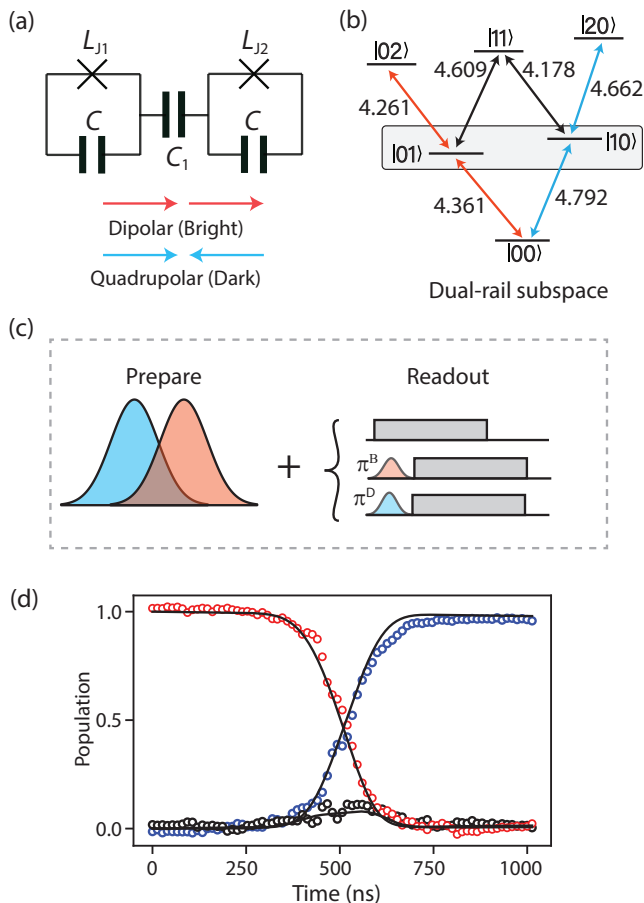


FIG. 3. (a): **Device concept and resonant-STIRAP:** (a) Schematic of the device showing two nearly resonant capacitively coupled transmons. The strong coupling between the two transmons results in a dipolar and a quadrupolar modes. (b) An experimentally determined energy-level diagram showing different transitions in the 2-qubit manifold. The orange(cyan) arrows depict the dipolar (quadrupolar) mode. The single excitation states in dipolar and quadrupolar modes *i.e.* $|01\rangle$ and $|10\rangle$ along with the ground state $|00\rangle$ ($|g\rangle$) form a “V-system” configuration for the coupled transmon system. The dual-rail subspace is spanned by $|01\rangle$ ($|0\rangle$) and $|10\rangle$ ($|1\rangle$). (c) The pulse protocol scheme for the demonstration of resonant-STIRAP in the time domain. The preparation pulse length is varied by truncating it at different times before the readout. For a given preparation, three separate measurements are done to determine the populations in three levels. (d) Time evolution of the populations of different levels during resonant STIRAP, showing the transfer of population from $|0\rangle$ to $|1\rangle$.

included in the supplemental materials. For the readout of these two-qubit modes, we use a 3D cavity and align the dipolar mode in the direction of the electric field of the fundamental cavity mode. Due to this alignment, the dipolar mode couples strongly to the cavity field, resulting in “bright mode” (called qubit- B from here on). However, the quadrupolar mode remains protected from

the cavity field in the first order (called as “Dark” or qubit- D from hereon). A strong ZZ -coupling between the two modes results in different dispersive shifts for the two modes and allows us to perform joint state readout [27].

We begin with single-tone cavity spectroscopy and determine the dressed cavity frequency $\tilde{\omega}_r/2\pi = 7.215$ GHz and a linewidth of $\kappa/2\pi \simeq 1$ MHz. We perform two-tone spectroscopy to determine all the transitions in two coupled transmon manifold as shown in Fig. 3(b). From two-tone spectroscopy, we determine the anharmonicities of both modes to be $\alpha_B/2\pi \simeq 100$ MHz and $\alpha_D/2\pi \simeq 130$ MHz, respectively. The time-domain characterization yields the coherences of $T_1 = 64 \mu\text{s}$ and $T_2^R = 106 \mu\text{s}$, for the B-mode, and $T_1 = 88 \mu\text{s}$ and $T_2^R = 98 \mu\text{s}$ for D mode. A detailed characterization of the device is included in the supplemental material.

Resonant STIRAP

We begin with the demonstration of resonant STIRAP for the population transfer from $|0\rangle$ to $|1\rangle$ within the 3 lowest levels of the system, as shown in Fig. 3(b). First, the state $|0\rangle$ is prepared using π pulse in the qubit-B manifold. For the resonant-STIRAP demonstration, we use two Gaussian pulses, each with a duration of 825 ns and a standard deviation of 133 ns. These pulses have equal amplitudes ($\Omega_0 = \Omega_1$) and a time-offset of 206 ns. Here, time offset denotes the time delay between the Gaussian pulses. To measure the time evolution of the population, these pulses can be truncated and immediately followed by a readout pulse. To measure the populations in the higher levels $|0\rangle$, and $|1\rangle$, we transfer the population from these states to the ground state $|g\rangle$ using π pulses on qubit-B and qubit-D, respectively [27]. The pulse sequence schematic is shown in Fig. 3(c).

The results from these measurements are shown in Fig. 3(d). For the resonant-STIRAP composite pulses of duration of $1 \mu\text{s}$, we observe that the transfer process is not quite adiabatic, ending up populating $|g\rangle$ state partially during the transfer. To understand our observations, we numerically model the system formed by three-levels and based on the experimental parameters. In these calculations, the decoherence errors are included as they become non-negligible due to the longer pulse length. We find that nearly 98 % population transfer and approximately 2 % population decay to ground state due to relaxation during the evolution.

Detuned STIRAP

To demonstrate detuned STIRAP for π and $\pi/2$ rotations, we begin by the phase and amplitude calibrations. We set a moderate single-photon detuning of 15 MHz.

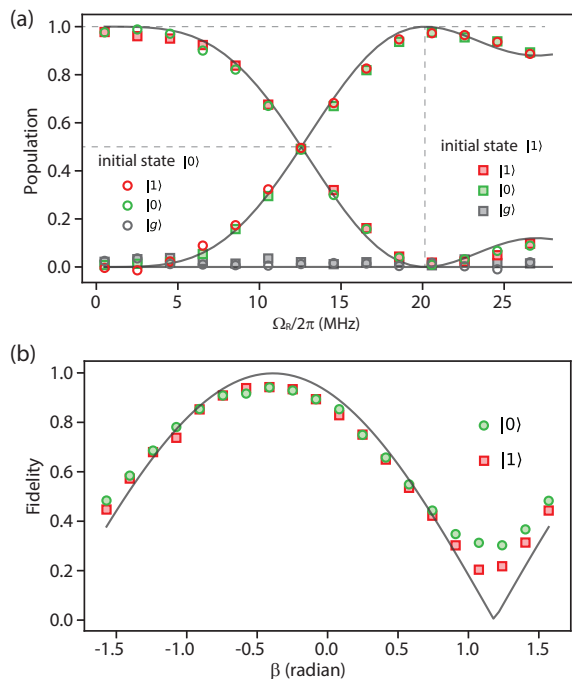


FIG. 4. **Calibration of the π and $\pi/2$ rotations:** (a) Populations in the three states while varying the amplitude $\Omega_R = \Omega_0 = \Omega_1$ of the detuned STIRAP pulses. Results for both the initial states $|0\rangle$ and $|1\rangle$ are shown. For these measurements, a detuned STIRAP pulse sequence of 260 ns duration is applied. (b) shows the calibration for the removal of the dynamical phase. The overlap of prepared state with $(|0\rangle + |1\rangle)/\sqrt{2}$ is plotted while varying the phase of detuned STIRAP pulses by the same amount simultaneously. Solid-lines are numerically computed results using experimentally determined device and pulse parameters. Note that the solid-lines corresponding to each initial state lie on top of each other and are not separately visible.

A pulse configuration, schematically shown in Fig. 1(b), having duration of 206 ns, $\sigma = 33$ ns, offset of 54 ns and equal Rabi amplitudes are used. We first prepare one of two initial states, $|0\rangle$ or $|1\rangle$. It is followed by a detuned STIRAP pulse sequence and then the sequences measuring the populations in all the states (as described earlier). Such a sequence is repeated while varying the amplitudes of the detuned STIRAP pulses. Fig. 4(a) shows the experimental results showing that with an amplitude of approximately 20 MHz, one can successfully swap the populations from $|0\rangle \rightarrow |1\rangle$ and $|1\rangle \rightarrow |0\rangle$ using the same pulse amplitude and without populating the state $|g\rangle$. Such a calibration, therefore can be used to implement π rotations in the qubit-subspace.

We further note that the intersection of the two curves showing the transfer for the two initial states ($|0\rangle$ and $|1\rangle$) takes place at a population of 0.5. It immediately suggests that half rotations can be implemented by simply controlling the amplitude of detuned STIRAP pulse. To correct any dynamical phase acquired during the de-

tuned STIRAP process and align the axes of rotation to the lab-frame, we next vary the phase of the microwave drives. The pulse amplitude is kept fixed to value corresponding to the common intersection point of half the population. It represents a superposition state with equal probability amplitudes *i.e.* $(|0\rangle + e^{i\gamma}|1\rangle)/\sqrt{2}$, where γ is the dynamical phase that needs to be determined and corrected to get the desired quantum state. We then perform quantum state-tomography of the prepared state (detailed in the next section) and compute its overlap with $(|0\rangle + |1\rangle)/\sqrt{2}$.

Fig. 4(b) shows the resultant fidelity as the phase of the microwave pulses is varied. The phase corresponding to the maximum fidelity represents a $\pi/2$ rotation about the y -axis. Thus, from these two calibrations, we can completely fix the amplitudes and phases required to implement half- and full-rotations about the x -, and y -axes on the Bloch-sphere spanned in the dual-rail subspace. The solid lines in Fig. 4 are numerically calculated using the experimentally determined device and pulse parameters.

Quantum state tomography (QST) of entire “V-shape” system

To further benchmark and check the completeness of the gates constructed using π and $\pi/2$ rotations, we experimentally measure the complete density matrix corresponding to the 3-level system using three-level quantum state tomography [27]. To perform a comprehensive QST, a complete set of nine independent measurements are carried out after preparation of a given state and calculating the density matrix based on the measurement outcomes. Before the measurements, we rotate the state by applying 9 different rotations consisting of different π and $\pi/2$ rotations *i.e.*, $\hat{R}_k = \{I, (\frac{\pi}{2})_x^{g0}, (\frac{\pi}{2})_y^{g0}, (\pi)_x^{g0}, (\frac{\pi}{2})_x^{g1}, (\frac{\pi}{2})_y^{g1}, (\pi)_x^{g0}(\frac{\pi}{2})_x^{g1}, (\pi)_x^{g0}(\frac{\pi}{2})_y^{g1}, (\pi)_x^{g0}(\pi)_x^{g1}\}$, where I denotes the identity and $(\theta)_a^{ij}$ denotes θ -rotation about a -axis between i, j transitions.

The measurement operator is given by $\hat{M}_i = \alpha_g(t)|g\rangle\langle g| + \alpha_0(t)|0\rangle\langle 0| + \alpha_1(t)|1\rangle\langle 1|$, where $\alpha_i(t)$ denotes the averaged transmitted field amplitudes for the state i . For each of these unitary rotations, we measure the coefficients $\langle I_k \rangle = \text{Tr}(\rho R_k \hat{M}_i \hat{R}_k^\dagger)$ by integrating the phase quadrature of the transmitted signal over the measurement time t . We then solve the linear equations $\text{Tr}(\rho_{\text{est}} R_k \hat{M}_i \hat{R}_k^\dagger) = \langle I_k \rangle_{\text{meas}}$ to reconstruct the density matrix ρ_{est} . The reconstructed density matrices ρ_{est} are post-processed using a maximum likelihood estimation procedure [28, 29].

Fig. 5 summarizes the experimentally obtained density matrices for four different states. Experimentally, we first initialize the system in state $|0\rangle$ or $|1\rangle$ by exciting it from the ground state. It is followed by a calibrated detuned

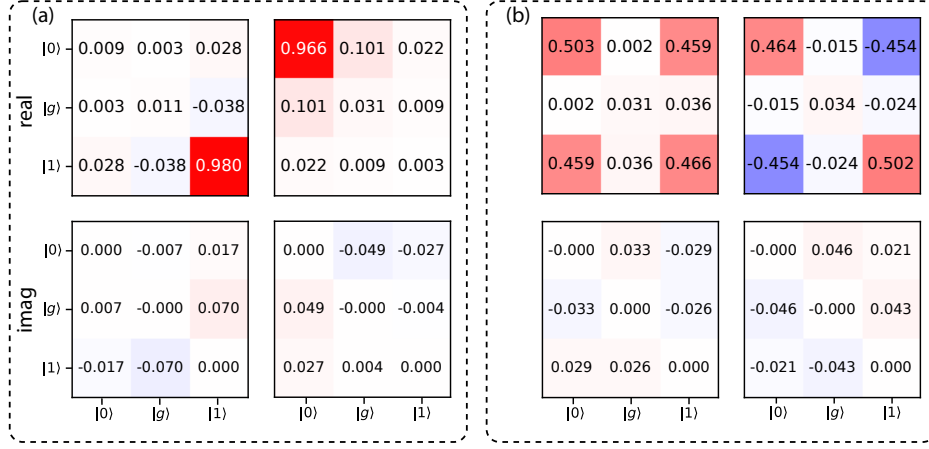


FIG. 5. **Quantum state tomography for different initial states $|0\rangle$ (left) and $|1\rangle$ (right) for both π and $\pi/2$ gates:** a) Real and imaginary plot of density matrix for π gate. b) Real and imaginary plot of density matrix for $\pi/2$ gate. The fidelities of the four target states are 0.990, 0.983, 0.971, and 0.967, each with an error margin of 0.7% in measurement.

STIRAP pulse corresponding to π or $\pi/2$ rotations, and subsequently by the state tomography sequences. When starting with $|0\rangle$ or $|1\rangle$, the system ends up in state $|1\rangle$ or $|0\rangle$ when a detuned STIRAP based π rotation about the y -axis is applied. Similarly, equal superposition states are prepared with the application of $\pi/2$ rotation about the y -axis while initializing the system in $|0\rangle$ or $|1\rangle$.

Robustness of the detuned STIRAP based rotation

To demonstrate the robustness of rotations with respect to deviations in the pulse amplitude and frequency, we target to prepare states $|1\rangle$ and $(|0\rangle + |1\rangle)/\sqrt{2}$ by the application of π and $\pi/2$ rotations about y -axis after initializing the system to state $|0\rangle$. We carry out the three-level quantum state tomography as described earlier and compute the fidelity of the prepared states while varying the pulse amplitudes and frequency and compare the results with numerical simulations based on experimentally determined parameters. Fig. 6 summarizes the experimental and numerical results for both π and $\pi/2$ rotations. The experimental data indicate that both rotations are somewhat resilient to deviations in amplitude and frequency. Whereas the numerically simulated plots remain relatively flat with respect to small deviations in the pulse parameters.

There are several potential sources for the discrepancy between the experimental and theoretical results. First, we use a 15 MHz single-photon detuning in the experiments, which introduces non-adiabatic effects and can degrade the target state fidelity. Second, the errors corresponding to the state preparation and the errors in the calibration of the gates used in tomography also contribute. For the experimental results shown in Fig. 6, we have not removed any state preparation, measurement,

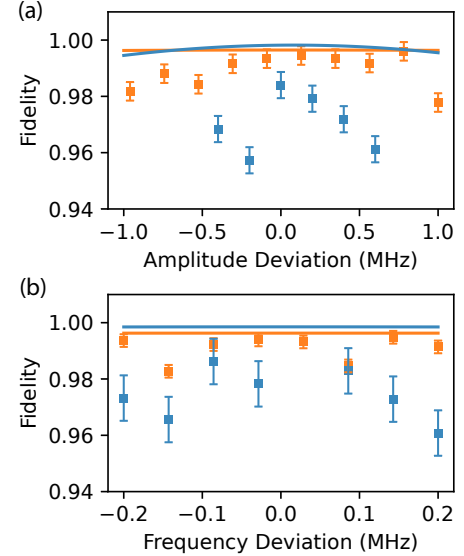


FIG. 6. **Robustness of π and $\pi/2$ rotations with respect to pulse amplitude and detuning:** The solid lines represents the numerical simulations and scatter points show the experimental data. (a) Robustness of gates with respect to amplitude error for π (orange) and $\pi/2$ (blue). (b) Robustness of gates with respect to detuning error for π (orange) and $\pi/2$ (blue).

and decoherence errors. On the technical side, a single microwave vector signal generator has been used to generate the control pulses for both the STIRAP pulses using a single sideband modulation technique. Due to pulse distortion and different pulse offsets, the calibration of the different rotations could have small error, which ultimately lowers the target state fidelities. Pulse optimization [30–33] and shortcut to adiabaticity techniques

[34, 35] can be employed to achieve higher state fidelities. Additional numerical analysis (detailed in the supplementary materials) reveals that employing a single-photon detuning greater than 15 MHz could result in a preparation state fidelity in excess of 0.999. Within this parameter range, the gates could perform approximately 5% better than typical resonant dynamical gates.

To summarize, we demonstrate detuned STIRAP inspired single qubit rotations in a dual-rail qubit formed by two fixed frequency transmons. We show that these gates are resilient to amplitude and detuning errors simultaneously when compared to the resonant pulse based rotations. While we use state-fidelity as the performance metric to check the robustness of these rotations with pulse amplitudes and frequency, it can be better understood by implementing quantum process tomography and randomized benchmarking protocols in the future.

Acknowledgment

The authors acknowledge the support under the CoE-QT program by MEITY and QuEST program by DST, Govt. of India (GoI). The authors acknowledge device fabrication facilities at CeNSE, IISc Bangalore, and central facilities at the Department of Physics funded by DST (GoI). U.S. acknowledge the support received through the PMRF (GoI).

APPENDIX A: DEVICE

Summary of the key device parameters

TABLE I. Device parameters

Parameter	Symbol	Value	Units
Dressed cavity frequency	$\tilde{\omega}_r/2\pi$	7.205	GHz
Cavity line width	$\kappa/2\pi$	1	MHz
Bright mode qubit frequency	$\tilde{\omega}_B/2\pi$	4.361	GHz
Dark mode qubit frequency	$\tilde{\omega}_D/2\pi$	4.792	GHz
Relaxation time of bright mode	$T_1(B)$	64	μs
Relaxation time of dark mode	$T_1(D)$	88	μs
Ramsey fringe time of bright mode	$T_2^R(B)$	106	μs
Ramsey fringe time of dark mode	$T_2^R(D)$	98	μs
Anharmonicity of bright mode	$\alpha_b/2\pi$	100	MHz
Anharmonicity of dark mode	$\alpha_d/2\pi$	130	MHz
Longitudinal coupling	$g_{zz}/2\pi$	180	MHz
Dispersive shift of bright mode	$\chi_b/2\pi$	1.2	MHz
Dispersive shift of dark mode	$\chi_d/2\pi$	1.55	MHz
Coupling of bright mode to cavity	$g_b/2\pi$	150	MHz
Junction asymmetry parameter	d_J	0.01	

Device fabrication

The 3D transmon qubits are fabricated on *c*-plane double-side polished 330 μm thick sapphire substrates. The transmon capacitor pads are made up of tantalum (Ta), and the Josephson junctions are fabricated using Al-AlO_x-Al. We grow 45 nm Ta films using the DC-magnetron sputtering process. We use an argon flow of 40 sccm, DC power of 250 W. The distance between the target and substrate holder is set at 180 mm, while the substrate holder is maintained at a temperature of 600° C. Additionally, the substrate rotation speed is set to 10 rpm. The sputtering pressure is maintained at 3 mTorr. These specified conditions collectively contribute to the controlled and optimized sputtering deposition process.

For the fabrication of Josephson junctions, we employ a double-layer resist stack to craft Manhattan-style junctions. Initially, we spin coat EL-11 and bake it for 5 minutes. Subsequently, we spin coat a second layer of ARP-6200 resist, followed by a 5-minute baking process. Finally, we top it off by coating a layer of a water-soluble discharging layer onto the resist stack to mitigate any potential charging issues during the lithography process. After exposure, we remove the anti-charging layer by dipping the chip in DI water for 60 seconds. Next, we remove the exposed ARP-6200 resist by using CSAR as a developer and IPA as a stopper. Finally, we remove the exposed EL-11 by using 1:3 ratio of MIBK:IPA as a developer and IPA as a stopper.

After development, the oxygen plasma is carried out for 40 seconds to remove the residual resist. The chip is then loaded into the electron beam evaporator. Before aluminum deposition, a crucial step is to remove the native oxide of tantalum through Ar-ion milling. The ion milling process involves specific parameters, including an Argon flow of 5 sccm, a beam voltage of 400 V, an accelerating voltage of 90 V, a beam current of 15 mA, a neutralizer emission current of 15 mA, and a duration of 40 seconds.

Following the ion milling, the next step involves depositing 15 and 30 nm of aluminum from two different directions with an intermediate oxidation step (2 Torr for 20 minutes). After the completion of deposition, the chip is kept in N-Methylpyrrolidone (NMP) solution for 3 hours at a temperature of 80°C before performing the liftoff. An optical microscope image of the fabricated device is shown in Fig. 7(a).

Measurement setup

The samples are cooled down using a BlueFors BF-LD250 dilution refrigerator with a base temperature of 12 mK. The samples are attached to a flange connected to the lowest temperature stage, which is directly cooled

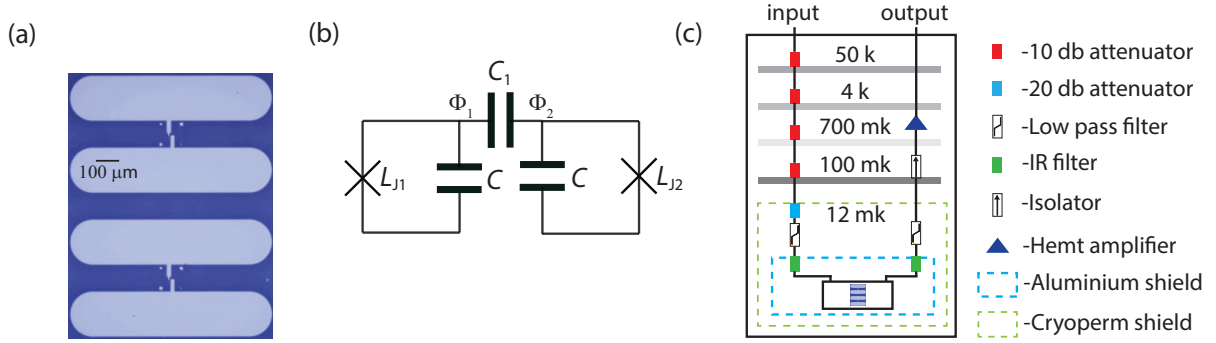


FIG. 7. **Device and measurement setup:** (a) An optical microscope image of a coupled transmon device. (b) An effective lumped element model of the two qubits showing node fluxes. (c) A schematic of the measurement setup showing various microwave components on the input and output lines. The low pass tubular filter (K&L 6L250-8000/T20000) and an isolator (LNF-ISC4.8A) from Low Noise Factory are used. Two stages of shielding protect the sample. The first stage is an aluminum shield coated with a mixture of carbon lampblack and silicon carbide grit to protect the device against IR radiation. The second stage is a cryo-perm shield for protection against the magnetic field.

down by the dilution process in the mixing chamber. Various components, such as attenuators, filters, amplifiers, and isolators at various stages are shown in Fig. 7(c). The control pulse and the measurement pulse are combined at room temperature, and the combined signal is sent to the input port of the cavity by using a single coaxial line. The output measurement pulse from the cavity is first sent through HEMT, followed by another amplifier at room temperature.

APPENDIX B: HAMILTONIAN OF TWO STRONGLY COUPLED TRANSMON

We start from the classical Lagrangian L of the circuit as shown in Fig. 7(b), showing the generalized flux variables at the left and right nodes of the circuit denoted by Φ_1 and Φ_2 . The kinetic energy K , stored in the capacitors can be written as,

$$K = \frac{C}{2} \dot{\Phi}_1^2 + \frac{C}{2} \dot{\Phi}_2^2 + \frac{C_c}{2} (\dot{\Phi}_1 - \dot{\Phi}_2)^2 \quad (8)$$

Similarly, we can write the potential energy U , stored in the junctions as,

$$U = -E_J (1 - d_J) \cos\left(\frac{\Phi_1}{\phi_0}\right) - E_J (1 + d_J) \cos\left(\frac{\Phi_2}{\phi_0}\right), \quad (9)$$

where $d_J = (E_{J2} - E_{J1}) / (E_{J2} + E_{J1})$ is an asymmetry parameter in the junctions in the Junction and $E_J = (E_{J2} + E_{J1}) / 2$ is the average Josephson energy, Φ is the node flux and $\phi_0 = \Phi_0 / 2\pi = \hbar / 2e$ is the reduced magnetic flux quantum. It is convenient to introduce “bright” and “dark” variables Φ_b and Φ_d as the flux average $\Phi_b = (\Phi_1 - \Phi_2) / 2$ and $\Phi_d = (\Phi_1 + \Phi_2) / 2$.

Now, the Lagrangian $L = K - U$ can be defined as,

$$L = C \dot{\Phi}_d^2 + (C + 2C_1) \dot{\Phi}_b^2 + 2E_J \left[\cos\left(\frac{\Phi_b}{\phi_0}\right) \cos\left(\frac{\Phi_d}{\phi_0}\right) \right] + 2E_J d_J \left[\sin\left(\frac{\Phi_b}{\phi_0}\right) \sin\left(\frac{\Phi_d}{\phi_0}\right) \right]. \quad (10)$$

We now calculate the conjugate charges Q_b and Q_d , corresponding to the phases Φ_b and Φ_d as,

$$Q_b = \frac{\partial L}{\partial \dot{\Phi}_b} = (2C + 4C_1) \dot{\Phi}_b \quad (11)$$

$$Q_d = \frac{\partial L}{\partial \dot{\Phi}_d} = 2C \dot{\Phi}_d \quad (12)$$

Now, we can obtain the Hamiltonian of the circuit

$$H(Q_b, Q_d, \Phi_b, \Phi_d) = Q_b \dot{\Phi}_b + Q_d \dot{\Phi}_d - L$$

as,

$$H = \frac{Q_b^2}{2C_b} + \frac{Q_d^2}{2C_d} - 2E_J \cos\left(\frac{\Phi_b}{\phi_0}\right) \cos\left(\frac{\Phi_d}{\phi_0}\right) - 2E_J d_J \sin\left(\frac{\Phi_b}{\phi_0}\right) \sin\left(\frac{\Phi_d}{\phi_0}\right), \quad (13)$$

where the effective capacitances are $C_b = 2C + 4C_1$ and $C_d = 2C$, respectively. We can now quantize this Hamiltonian by promoting the flux and charge variables to operators. In addition, we define dimensionless phase operators $\hat{\varphi}_j = \hat{\Phi}_j / \phi_0$ and charge number operators $\hat{n}_j = \hat{Q}_j / 2e$, and use them to express the quantum Hamiltonian of the circuit as,

$$H = 4\hat{n}_b^2 E_{C_b} + 4\hat{n}_d^2 E_{C_d} - 2E_J \cos \hat{\varphi}_b \cos \hat{\varphi}_d - 2E_J d_J \sin \hat{\varphi}_b \sin \hat{\varphi}_d. \quad (14)$$

We define $E_{C_b} = e^2/(2C_b)$ and $E_{C_d} = e^2/(2C_d)$ as the charging energy corresponding to the dark and bright mode, respectively. In the low anharmonicity limit, $\hat{\phi}_a, \hat{\phi}_b \ll 1$, we can expand the cosines and retain the terms up to 4th order in the phases. Also, if the junctions are nearly identical $d_J \ll 1$, we can simplify the Hamiltonian by taking $d_J = 0$ as it will only add small unwanted coupling terms between the qubits [36]. By taking into account the above approximations we can finally write the Hamiltonian as,

$$\begin{aligned} \hat{H} = & 4E_{C_b}\hat{n}_b^2 + \frac{E_{J_b}}{2}\hat{\varphi}_b^2 - \frac{E_J}{12}\hat{\varphi}_b^4 + 4E_{C_d}\hat{n}_d^2 \\ & + \frac{E_{J_d}}{2}\hat{\varphi}_d^2 - \frac{E_J}{12}\hat{\varphi}_d^4 - \frac{E_J}{2}\hat{\varphi}_b^2\hat{\varphi}_d^2 + \mathcal{O}(6), \end{aligned} \quad (15)$$

where $E_{J_b} = E_{J_d} = 2E_J$. By defining the annihilation and creation operators corresponding to both the modes as follows,

$$\hat{\varphi}_b = \left(\frac{8E_{C_b}}{E_{J_b}}\right)^{1/4} \frac{\hat{b} + \hat{b}^\dagger}{\sqrt{2}} \quad (16)$$

$$\hat{n}_b = -i \left(\frac{E_{J_b}}{8E_{C_b}}\right)^{1/4} \frac{\hat{b} - \hat{b}^\dagger}{\sqrt{2}} \quad (17)$$

$$\hat{\varphi}_d = \left(\frac{8E_{C_d}}{E_{J_d}}\right)^{1/4} \frac{\hat{d} + \hat{d}^\dagger}{\sqrt{2}} \quad (18)$$

$$\hat{n}_d = -i \left(\frac{E_{J_d}}{8E_{C_d}}\right)^{1/4} \frac{\hat{d} - \hat{d}^\dagger}{\sqrt{2}}, \quad (19)$$

we can reduce the Hamiltonian as,

$$\begin{aligned} H = & \tilde{\omega}_b b^\dagger b - \frac{\alpha_b}{2} b^\dagger b^\dagger b b + \tilde{\omega}_d d^\dagger d \\ & - \frac{\alpha_d}{2} d^\dagger d^\dagger d d - 2g_{zz} b^\dagger b d^\dagger d, \end{aligned} \quad (20)$$

where $\alpha_b = E_{C_b}$, $\alpha_d = E_{C_d}$, $g_{zz} = \sqrt{E_{C_b}E_{C_d}}$, $\tilde{\omega}_b = \sqrt{8E_{J_b}E_{C_b}} - \alpha_b - g_{zz}$, and $\tilde{\omega}_d = \sqrt{8E_{J_d}E_{C_d}} - \alpha_d - g_{zz}$. These expressions represent two transmon qubits which are strongly coupled to each other by a longitudinal coupling g_{zz} .

Coupling of qubits with cavity

For the joint-state readout of both the ‘‘qubits’’, we couple them to a 3D microwave copper cavity. The coupled Hamiltonian of such a three mode system can be expressed as,

$$\begin{aligned} H = & \omega_r a^\dagger a + \tilde{\omega}_b b^\dagger b - \frac{\alpha_b}{2} b^\dagger b^\dagger b b + \tilde{\omega}_d d^\dagger d \\ & - \frac{\alpha_d}{2} d^\dagger d^\dagger d d - 2g_{zz} b^\dagger b d^\dagger d \\ & + g_b(a^\dagger b + ab^\dagger) + g_d(a^\dagger d + ad^\dagger), \end{aligned} \quad (21)$$

where ω_r represents the bare frequency of the readout cavity and $g_b(g_d)$ represents its coupling to the bright

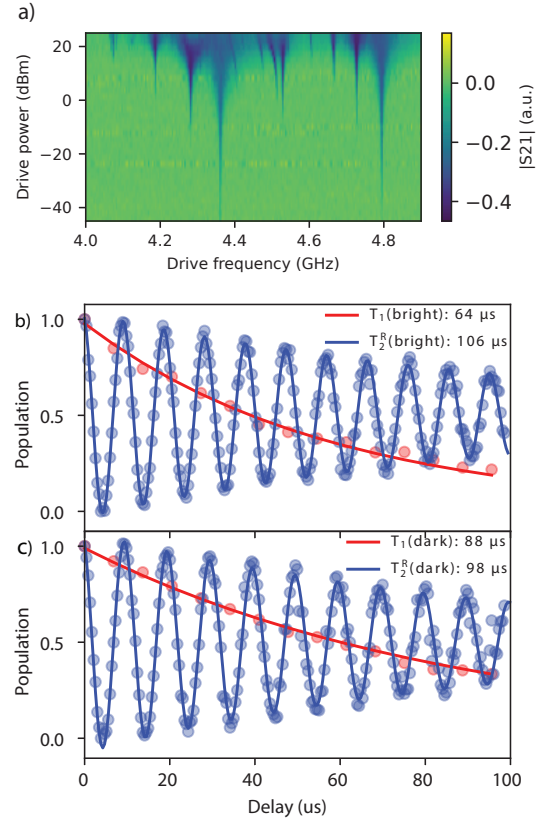


FIG. 8. **Qubits spectroscopy and coherence:** (a) Two tone spectroscopy showing the coupled qubit spectrum as the drive tone frequency and its strength are varied. Higher transitions in the coupled qubit manifold (including multi-photon transitions) can also be seen. (b, c) Energy relaxation and Ramsey-fringe measurements for the bright and dark modes.

(dark) mode. The bright mode is attributed to the dipolar mode due to its alignment with the fundamental modes, the cavity and it couples strongly to the cavity. The dark mode is attributed to the quadrupole mode of oscillation, and it does not couple to the cavity as strongly. Therefore, for the simplification, we set the dipolar coupling of the dark mode to zero *i.e.* $g_d = 0$.

After finding the eigenenergies using the non-degenerate perturbation theory [37], the dispersive shifts corresponding to both modes can be calculated as,

$$\chi_b = \frac{2g_b^2\alpha_b}{\Delta_b(\alpha_b - \Delta_b)} \quad (22)$$

$$\chi_d = \frac{2g_b^2g_{zz}}{\Delta_b(2g_{zz} - \Delta_b)} \quad (23)$$

It is interesting to point out that the dark (quadrupole) mode mostly remains decoupled from the cavity, therefore does not directly contribute to the dispersive shift. However, due to the strong cross-Kerr interaction between the qubit modes, the dispersive shift of the dark

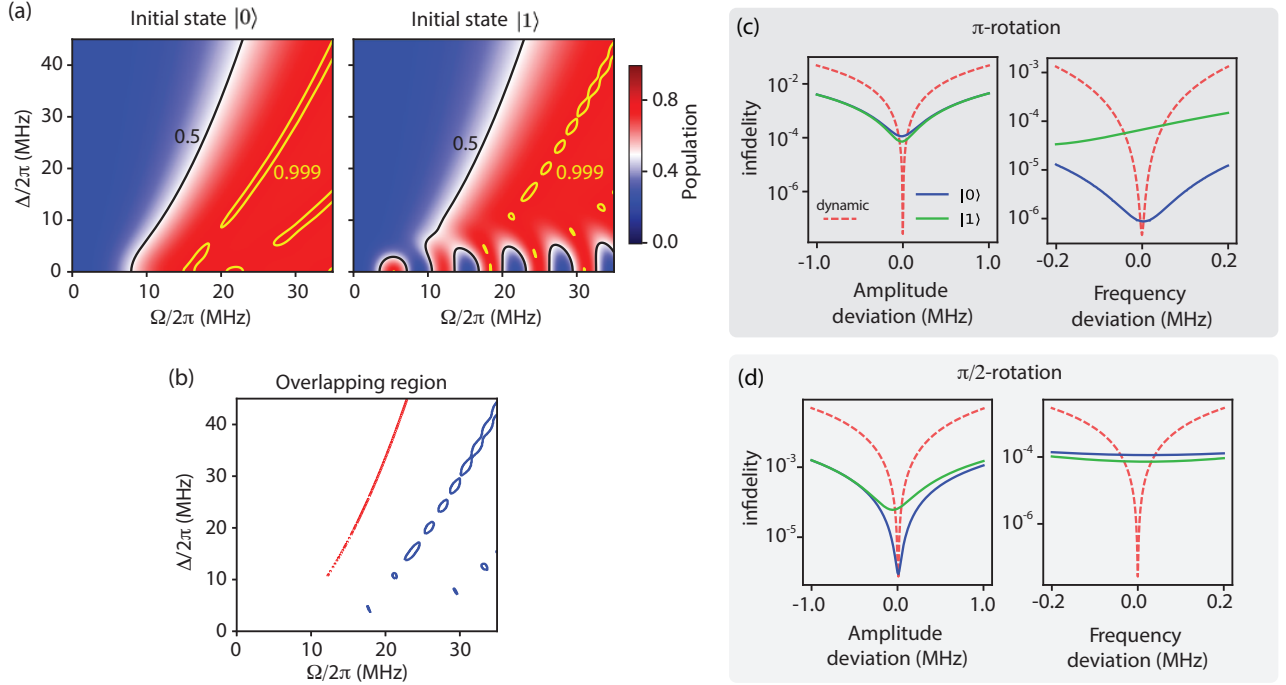


FIG. 9. (a) Numerically calculated plot of the population in $|1\rangle$ (left panel) after the end of the detuned STIRAP pulse with an initial state of $|0\rangle$. The right panel shows the results from similar calculations and plot the population in $|0\rangle$ with an initial state of $|1\rangle$. (b) Plot shows the common regions in the parameter space for which detuned STIRAP protocol prepare an equal superposition (red) or the complete transfer (blue) within an error tolerance of 10^{-3} . (c) Panel shows the numerically calculated state infidelity for the π rotation with respect to the deviation in the pulse amplitude and frequency around the optimum point. The blue (green) line represents the result when the system is prepared in the initial state $|0\rangle$ ($|1\rangle$). The state infidelity is calculated using the target state $|1\rangle$ ($|0\rangle$). (d) Panel shows the state infidelity for the $\pi/2$ rotation with respect to deviation in amplitude/frequency around the optimum point. For an initial state of $|0\rangle$, the infidelity is computed using the target state of $(|0\rangle + |1\rangle)/\sqrt{2}$ and is shown with blue line. Similarly, the green line represents the result, when the system is initially prepared in state $|1\rangle$ and final state is measured in state $(|0\rangle - |1\rangle)/\sqrt{2}$. For comparison, similar results are obtained by using dynamic rotations are also included (red-dashed line).

mode depends on the cross-kerr coupling. In the dispersive limit, the Hamiltonian can be simplified to

$$\begin{aligned}
 H = & \tilde{\omega}'_b b^\dagger b + \tilde{\omega}_d d^\dagger d + \tilde{\omega}_r a^\dagger a - \frac{\alpha_b}{2} b^\dagger b^\dagger b b \\
 & - \frac{\alpha_d}{2} d^\dagger d^\dagger d d + \chi_b a^\dagger a b^\dagger b \\
 & + \chi_d a^\dagger a d^\dagger d - 2g_{zz} b^\dagger b d^\dagger d,
 \end{aligned} \quad (24)$$

where $\tilde{\omega}'_b = \tilde{\omega}_b + \frac{g_b^2}{\Delta_b}$ and $\tilde{\omega}_r = \omega_r - \frac{g_b^2}{\Delta_b}$

APPENDIX C: DEVICE CHARACTERIZATION

To determine the transition frequencies for both qubit modes, we begin with the two-tone spectroscopy method. The cavity is continuously probed at the dressed frequency of 7.215 GHz while varying the frequency of an excitation tone applied near the expected qubit transitions. Fig. 8(a) show the results from the two-tone spectroscopy measurements. It is evident that at very low drive power, only two modes persist, revealing qubit mode frequen-

cies of 4.361 GHz and 4.792 GHz. The drive power in Fig. 8(a) refers to the signal generator's output. After the initial spectroscopic characterization, we carry out time domain coherence measurements. Fig. 8 (b, c) shows the coherence measurements for both the qubit modes. We emphasize here that based on the simulations, the energy relaxation rate for the bright mode is Purcell-factor limited. The dark mode remains uncoupled from the readout cavity, so it shows a somewhat larger energy relaxation time. In Table I, we summarize the various parameters of the device.

APPENDIX D: NUMERICAL RESULTS OF DETUNED STIRAP BASED ROTATIONS

To study detuned STIRAP-based rotations to implement it as a quantum gate, we introduce single-photon detuning to lift the degeneracies in instantaneous eigenvalues. Using QuTiP, we solve the time-dependent Lindblad master equation to simulate the evolution of the

system under the time-dependent Hamiltonian described by Eq. 1 of the main text. Our investigation focuses on understanding how single-photon detuning Δ and drive amplitude Ω affects the final state. We analyze this evolution across different parameter settings and the two initial states, namely $|0\rangle$ and $|1\rangle$. We use Gaussian pulses of the total duration of 206 ns, standard deviation of σ of 40 ns, an offset of 54 ns, and of equal amplitudes.

The left panel of Fig. 9(a) shows the population in $|1\rangle$ for an initial state $|0\rangle$ when subjected to a 260 ns (206 ns + 54 ns) while varying the single-photon detuning and amplitude. Similarly, the right panel shows the population in $|0\rangle$ for an initial state $|1\rangle$. In these panels, the solid black lines indicate the contour corresponding to the population of 0.5. The yellow lines denote regions where the population at the end of the operation reaches 0.999.

It is important to note that there are common regions in both the panels *i.e.* common values of the single-photon detuning and amplitude, where the equal superposition or the complete transfer can be achieved. Thus, these values of detuning and drive amplitude makes the rotations independent of the initial condition. Fig. 9(b) illustrate the common regions in both plots with a tolerance of 10^{-3} for the equal superpositions and complete transfer. This figure delineate specific regions where detuned STIRAP can be utilized for $\pi/2$ and π rotations.

Due to the finite-length of the detuned STIRAP pulses, their rotations are not perfect. To better understand these imperfections and their sensitivity to pulse parameters, we carry out QuTiP-based numerical calculations. Fig. 9(c, d) summarizes the results from these calculations. The top panel shows the infidelity of the prepared state after the application of π rotation while varying the amplitude and frequency of the detuned STIRAP pulses. Similar results for the $\pi/2$ rotations are shown in the bottom panel. For a comparison, we also plot the results for the standard dynamical rotations implemented by a resonant pulse driving the qubit subspace denoted by red dashed line. It is evident from the figure that while dynamical rotations can offer much lower errors, these are not enough robust with respect to frequency and amplitude deviations. The detuned STIRAP rotations exhibit robustness over a larger range of deviations in the pulse parameters. The minimum error introduced by the finite length detuned STIRAP can, in principle, be further reduced by increasing the single-photon detuning or employing techniques such as shortcuts to adiabaticity.

* v.singh@iisc.ac.in

[1] P. Zanardi and M. Rasetti, Holonomic quantum computation, *Physics Letters A* **264**, 94 (1999).
 [2] L.-M. Duan, J. I. Cirac, and P. Zoller, Geometric Manipulation of Trapped Ions for Quantum Computation,

Science **292**, 1695 (2001).
 [3] N. V. Vitanov, A. A. Rangelov, B. W. Shore, and K. Bergmann, Stimulated Raman adiabatic passage in physics, chemistry, and beyond, *Reviews of Modern Physics* **89**, 015006 (2017).
 [4] K. Bergmann, H.-C. Nägerl, C. Panda, G. Gabrielse, E. Miloglyadov, M. Quack, G. Seyfang, G. Wichmann, S. Ospelkaus, A. Kuhn, S. Longhi, A. Szameit, P. Pirro, B. Hillebrands, X.-F. Zhu, J. Zhu, M. Drewsen, W. K. Hensinger, S. Weidt, T. Halfmann, H.-L. Wang, G. S. Paraoanu, N. V. Vitanov, J. Mompart, T. Busch, T. J. Barnum, D. D. Grimes, R. W. Field, M. G. Raizen, E. Narevicius, M. Auzinsh, D. Budker, A. Pálffy, and C. H. Keitel, Roadmap on STIRAP applications, *Journal of Physics B: Atomic, Molecular and Optical Physics* **52**, 202001 (2019).
 [5] K. S. Kumar, A. Vepsäläinen, S. Danilin, and G. S. Paraoanu, Stimulated Raman adiabatic passage in a three-level superconducting circuit, *Nature Communications* **7**, 10628 (2016).
 [6] H. K. Xu, C. Song, W. Y. Liu, G. M. Xue, F. F. Su, H. Deng, Y. Tian, D. N. Zheng, S. Han, Y. P. Zhong, H. Wang, Y.-x. Liu, and S. P. Zhao, Coherent population transfer between uncoupled or weakly coupled states in ladder-type superconducting qutrits, *Nature Communications* **7**, 10.1038/ncomms11018.
 [7] A. Vepsäläinen, S. Danilin, and G. S. Paraoanu, Superadiabatic population transfer in a three-level superconducting circuit, *Science Advances* **5**, eaau5999 (2019).
 [8] J. Siewert, T. Brandes, and G. Falci, Adiabatic passage with superconducting nanocircuits, *Optics Communications Quantum Control of Light and Matter*, **264**, 10.1016/j.optcom.2005.12.083 (2006).
 [9] N. V. Vitanov, K.-A. Suominen, and B. W. Shore, Creation of coherent atomic superpositions by fractional stimulated Raman adiabatic passage, *Journal of Physics B: Atomic, Molecular and Optical Physics* **32**, 4535 (1999).
 [10] X. Lacour, N. Sangouard, S. Guérin, and H. R. Jauslin, Arbitrary state controlled-unitary gate by adiabatic passage, *Physical Review A* **73**, 042321 (2006).
 [11] I. I. Beterov, M. Saffman, E. A. Yakshina, V. P. Zhukov, D. B. Tretyakov, V. M. Entin, I. I. Ryabtsev, C. W. Mansell, C. MacCormick, S. Bergamini, and M. P. Fedoruk, Quantum gates in mesoscopic atomic ensembles based on adiabatic passage and Rydberg blockade, *Physical Review A* **88**, 010303 (2013).
 [12] G. T. Genov, S. Rochester, M. Auzinsh, F. Jelezko, and D. Budker, Robust two-state swap by stimulated Raman adiabatic passage, *Journal of Physics B: Atomic, Molecular and Optical Physics* **56**, 054001 (2023).
 [13] Z. Kis and F. Renzoni, Qubit rotation by stimulated Raman adiabatic passage, *Physical Review A* **65**, 032318 (2002).
 [14] D. Moller, L. B. Madsen, and K. Molmer, Geometric phase gates based on stimulated Raman adiabatic passage in tripod systems, *Physical Review A* **75**, 10.1103/PhysRevA.75.062302 (2007).
 [15] H. Ribeiro and A. A. Clerk, Accelerated adiabatic quantum gates: optimizing speed versus robustness, *Physical Review A* **100**, 032323 (2019).
 [16] F. Setiawan, P. Groszkowski, H. Ribeiro, and A. A. Clerk, Analytic Design of Accelerated Adiabatic Gates in Realistic Qubits: General Theory and Applications to Super-

- conducting Circuits, *PRX Quantum* **2**, 030306 (2021).
- [17] A. A. Abdumalikov Jr, J. M. Fink, K. Juliusson, M. Pechal, S. Berger, A. Wallraff, and S. Filipp, Experimental realization of non-Abelian non-adiabatic geometric gates, *Nature* **496**, [10.1038/nature12010](https://doi.org/10.1038/nature12010) (2013).
- [18] Y. Xu, Z. Hua, T. Chen, X. Pan, X. Li, J. Han, W. Cai, Y. Ma, H. Wang, Y. Song, Z.-Y. Xue, and L. Sun, Experimental Implementation of Universal Nonadiabatic Geometric Quantum Gates in a Superconducting Circuit, *Physical Review Letters* **124**, [10.1103/PhysRevLett.124.230503](https://doi.org/10.1103/PhysRevLett.124.230503) (2020).
- [19] T. Chen, Z.-Y. Xue, and Z. Wang, Error-Tolerant Geometric Quantum Control for Logical Qubits with Minimal Resources, *Physical Review Applied* **18**, 014062 (2022).
- [20] J. Howard, A. Lidiak, C. Jameson, B. Basyildiz, K. Clark, T. Zhao, M. Bal, J. Long, D. P. Pappas, M. Singh, and Z. Gong, Implementing two-qubit gates at the quantum speed limit, *Physical Review Research* **5**, 043194 (2023).
- [21] Z.-Y. Fang, H. Xu, T. Chen, K. Wei, and C. Zhang, Nonadiabatic geometric quantum gates by composite pulses based on superconducting qubits, *Physical Review A* **109**, [10.1103/PhysRevA.109.042615](https://doi.org/10.1103/PhysRevA.109.042615) (2024).
- [22] F. Setiawan, P. Groszkowski, and A. A. Clerk, Fast and Robust Geometric Two-Qubit Gates for Superconducting Qubits and beyond, *Physical Review Applied* **19**, [10.1103/PhysRevApplied.19.034071](https://doi.org/10.1103/PhysRevApplied.19.034071) (2023).
- [23] A. Kubica, A. Haim, Y. Vaknin, F. Brandão, and A. Retzker, *Erase qubits: Overcoming the T_1 limit in superconducting circuits* (2022).
- [24] H. Levine, A. Haim, J. S. Hung, N. Alidoust, M. Kalaei, L. DeLorenzo, E. A. Wollack, P. A. Arriola, A. Khalajhedayati, Y. Vaknin, *et al.*, Demonstrating a Long-Coherence Dual-Rail Erasure Qubit Using Tunable Transmons, *Physical Review X* **14**, 011051 (2024).
- [25] S. A. Caldwell, N. Didier, C. A. Ryan, E. A. Sete, A. Hudson, P. Karalekas, R. Manenti, M. P. da Silva, R. Sinclair, E. Acala, N. Alidoust, J. Angeles, A. Bestwick, M. Block, B. Bloom, A. Bradley, C. Bui, L. Capelluto, R. Chilcott, J. Cordova, G. Crossman, M. Curtis, S. Deshpande, T. E. Bouayadi, D. Girshovich, S. Hong, K. Kuang, M. Lenihan, T. Manning, A. Marchenkov, J. Marshall, R. Maydra, Y. Mohan, W. O'Brien, C. Osborn, J. Otterbach, A. Papageorge, J.-P. Paquette, M. Pelstring, A. Pollreno, G. Prawiroatmodjo, V. Rawat, M. Reagor, R. Renzas, N. Rubin, D. Russell, M. Rust, D. Scarbelli, M. Scheer, M. Selvanayagam, R. Smith, A. Staley, M. Suska, N. Tezak, D. C. Thompson, T.-W. To, M. Vahidpour, N. Vodrahalli, T. Whyland, K. Yadav, W. Zeng, and C. Rigetti, Parametrically Activated Entangling Gates Using Transmon Qubits, *Physical Review Applied* **10**, [10.1103/PhysRevApplied.10.034050](https://doi.org/10.1103/PhysRevApplied.10.034050) (2018).
- [26] J. R. Johansson, P. D. Nation, and F. Nori, QuTiP 2: A Python framework for the dynamics of open quantum systems, *Computer Physics Communications* **184**, 1234 (2013).
- [27] R. Bianchetti, S. Filipp, M. Baur, J. M. Fink, C. Lang, L. Steffen, M. Boissonneault, A. Blais, and A. Wallraff, Control and Tomography of a Three Level Superconducting Artificial Atom, *Physical Review Letters* **105**, 223601 (2010).
- [28] S. Filipp, P. Maurer, P. J. Leek, M. Baur, R. Bianchetti, J. M. Fink, M. Göppl, L. Steffen, J. M. Gambetta, A. Blais, and A. Wallraff, Two-Qubit State Tomography Using a Joint Dispersive Readout, *Physical Review Letters* **102**, [10.1103/PhysRevLett.102.200402](https://doi.org/10.1103/PhysRevLett.102.200402) (2009).
- [29] D. F. V. James, P. G. Kwiat, W. J. Munro, and A. G. White, Measurement of qubits, *Physical Review A* **64**, [10.1103/PhysRevA.64.052312](https://doi.org/10.1103/PhysRevA.64.052312) (2001).
- [30] W. Zheng, Y. Zhang, Y. Dong, J. Xu, Z. Wang, X. Wang, Y. Li, D. Lan, J. Zhao, S. Li, X. Tan, and Y. Yu, Optimal control of stimulated Raman adiabatic passage in a superconducting qubit, *npj Quantum Information* **8**, [10.1038/s41534-022-00521-7](https://doi.org/10.1038/s41534-022-00521-7) (2022).
- [31] G. S. Vasilev, A. Kuhn, and N. V. Vitanov, Optimum pulse shapes for stimulated Raman adiabatic passage, *Physical Review A* **80**, [10.1103/PhysRevA.80.013417](https://doi.org/10.1103/PhysRevA.80.013417) (2009).
- [32] J. Brown, S. Sgroi, L. Giannelli, G. S. Paraoanu, E. Paladino, G. Falci, M. Paternostro, and A. Ferraro, Reinforcement learning-enhanced protocols for coherent population-transfer in three-level quantum systems, *New Journal of Physics* **23**, [10.1088/1367-2630/ac2393](https://doi.org/10.1088/1367-2630/ac2393) (2021).
- [33] C. Zhang, Y. Liu, J. Song, Y. Xia, and Z.-C. Shi, High-fidelity quantum gates via optimizing short pulse sequences in three-level systems, *New Journal of Physics* **26**, [10.1088/1367-2630/ad1a2a](https://doi.org/10.1088/1367-2630/ad1a2a) (2024).
- [34] X. Chen, I. Lizuain, A. Ruschhaupt, D. Guéry-Odelin, and J. G. Muga, Shortcut to Adiabatic Passage in Two- and Three-Level Atoms, *Physical Review Letters* **105**, [10.1103/PhysRevLett.105.123003](https://doi.org/10.1103/PhysRevLett.105.123003) (2010).
- [35] H. L. Mortensen, J. J. W. H. Sørensen, K. Mølmer, and J. F. Sherson, Fast state transfer in a Λ -system: a shortcut-to-adiabaticity approach to robust and resource optimized control, *New Journal of Physics* **20**, [10.1088/1367-2630/aaac8a](https://doi.org/10.1088/1367-2630/aaac8a) (2018).
- [36] Susanne Richer, Nataliya Maleeva, Sebastian T. Skacel, Ioan M. Pop, and David DiVincenzo, "Inductively shunted transmon qubit with tunable transverse and longitudinal coupling," *Physical Review B* **96** (2017), [10.1103/PhysRevB.96.174520](https://doi.org/10.1103/PhysRevB.96.174520).
- [37] Gengyan Zhang, Yanbing Liu, James J. Raftery, and Andrew A. Houck, "Suppression of photon shot noise dephasing in a tunable coupling superconducting qubit," *npj Quantum Information* **3** (2017), [10.1038/s41534-016-0002-2](https://doi.org/10.1038/s41534-016-0002-2).